(Supporting Information)

Alkyl sulfonate surfactant mediates electroreduction of carbon dioxide to ethanol over hydroxide-derived copper catalysts

Yiding Wang[1,2], Runyao Zhao[1,2], Yunpeng Liu[3], Fengtao Zhang[2], Yuepeng Wang[1,2], Zhonghua Wu[2,3], Buxing Han [1,2] and Zhimin Liu*[1,2]

[1]Beijing National Laboratory for Molecular Sciences, CAS Laboratory of Colloid and Interface and Thermodynamics, CAS Research/Education Centre for Excellence in Molecular Sciences, Centre for Carbon Neutral Chemistry, Institute of Chemistry, Chinese Academy of Sciences, Beijing 100190, China; University of Chinese Academy of Sciences, Beijing 100049, P. R. China.

[2]University of Chinese Academy of Sciences, Beijing 100049, P. R. China.

[3]Institute of High Energy Physics, Chinese Academy of Sciences, Beijing 100049, China.

E-mail: liuzm@iccas.ac.cn

Table of Contents

Experimental Procedures 4

Materials 4

Sample characterizations 4

Electrochemical measurements 4

CO_2ER product analysis 4

Computational methods 4

Results and Discussion 6

Figure S1. Illustration of Cu@SDS preparation. 6

Figure S2. (a) SEM image, (b) TEM image and (c, d) HR-TEM images of $Cu(OH)_2$@SDS. 7

Figure S3. (a) SEM image, (b) TEM image and (c) HR-TEM image of $Cu(OH)_2$. 8

Figure S4. Cu 2p X-ray photoelectron spectroscopy (XPS) of $Cu(OH)_2$@SDS and $Cu(OH)_2$. 9

Figure S5. C 1s XPS of $Cu(OH)_2$@SDS and $Cu(OH)_2$. 10

Figure S6. XRD patterns of $Cu(OH)_2$@SDS and $Cu(OH)_2$. 11

Figure S7. FTIR spectra of $Cu(OH)_2$@SDS and $Cu(OH)_2$. 12

Figure S8. Raman spectra of $Cu(OH)_2$@SDS and $Cu(OH)_2$. 13

Figure S9. TG and DTG curves of $Cu(OH)_2$@SDS and $Cu(OH)_2$. 14

Figure S10. TG analysis curve of SDS. 15

Figure S11. Charge distribution of (a) DS^- and (b) OH^-. 16

Figure S12. LSV comparison of Cu@SDS (a) and OHDCu (b) under N_2 or CO_2. 17

Figure S13. The ratios of C_2/C_1 over Cu@SDS and OHDCu at different potentials. 18

Figure S14. FEs of the products from CO_2ER over mechanically mixed SDS and $Cu(OH)_2$ at different potentials. 19

Figure S15. ^{1}H NMR spectrum of liquid products of CO_2ER over Cu@SDS at 100 mA cm^{-2} for 3 h. 20

Figure S16. ^{1}H NMR spectrum of the anolyte with addition of ethanol into catholyte only, applying current density at 100 mA cm^{-2} for 3 h. 21

Figure S17. GC spectrum of the gas phase of CO_2ER over Cu@SDS at applied potential of -0.8 V. 22

Figure S18. ^{1}H NMR spectrum of liquid products of CO_2ER over Cu@SOS at -0.8 V. 23

Figure S19. ^{13}C NMR spectrum of liquid products with $^{13}CO_2$ as feedstock over Cu@SDS at -0.8 V. 24

Figure S20. SEM images of the catalysts evolved from $Cu(OH)_2$@SDS to Cu@SDS via electroreduction for desired time at -0.7 V. 25

Figure S21. SEM image of OHDCu. 26

Figure S22. XANES of Cu@SDS and OHDCu applied in CO_2ER at -0.9 V. 27

Figure S23. Difference charge density analysis given in isosurface graph. (a) Cu(111)@PS from Cu(111) and PS. (b) Charge distribution of Cu(111)@PS, (c) Cu(111) and (d) PS. 28

Figure S24. Structure of Cu(111)@PS before (a from ***b*** direction and b from ***c*** direction) and after (c from ***b*** direction and d from ***c*** direction) anchoring 2 Na atoms into Cu structure. 29

Figure S25. In situ FTIR spectra from 2800 cm^{-1} to 3000 cm^{-1} applying Cu@SDS as catalyst with potential applied from OCP, -0.1 V to -1.1 V. 30

Figure S26. Circumstantial catalytic route towards ethanol (lower) or ethylene (upper) generation on Cu@SDS or OHDCu. 31

Figure S27. Full version of reaction paths on Cu(111)@PS. (a) Cu(111)@PS, (b) Cu(111)@PS*HCCOH, (c) Cu(111)@PS*HCCHOH and (d) Cu(111)@PS*CCH. 32

Figure S28. Distance between H in *HCOOH and O from SDS. 33

Figure S29. Full version of reaction paths on Cu(111). (a) Cu(111), (b) Cu(111)*HCCOH, (c) Cu(111)*HCCHOH and (d) Cu(111)*CCH. 34

Figure S30. Cyclic voltammograms of Cu@SDS (a) and OHDCu (b). (c) Calculated C_{dl} according to (a, b). 35

Figure S31. The EIS data of Cu@SDS and OHDCu. 36

Figure S32. XRD pattern of OHDCu on Nafion-contained carbon paper. 37

i S33. XPS survey of $Cu(OH)_2$@SDS (a) and $Cu(OH)_2$ (b). 38

Figure S34. Picture of customized in situ FTIR accessary of ATR mode. 39

Table S1. Calculated energies of slabs and with adsorbed species. 40

Reference 41

Experimental Procedures

Materials

Cupric chloride ($CuCl_2$) was purchase from J&K Scientific. Potassium hydroxide (85%, KOH) and potassium bicarbonate were purchased from Sinopharm Chemical Reagent Co., Ltd. High-purity CO_2 (99.999 %) and N_2 (99.99 %) were supplied by Beijing Huayuan Gas Chemical Industry Co., Ltd. The alkyl sulfonate surfactants including sodium dodecyl sulfonate (SDS) and sodium octane sulfonate (SOS) were provided by Sinopharm Chemical Reagent Co., Ltd.

Sample characterizations

XRD analysis was performed on a Regaku D/Max-2500 (Rigaku Co., Japan) diffractometer equipped with Cu Kα1 radiation (λ = 1.54056 Å). X-ray photoelectron spectroscopy (XPS) was carried out on an X-ray photoelectron spectrometer (ESCALab 250Xi, Thermo Fisher Scientific, USA) using 200 W Al-Kα radiation. The base pressure was about 3 × 10^{-10} mbar, with 284.8 eV hydrocarbon C1s line from exogenous carbon as an energy reference. Fourier Transform Infrared (FTIR) spectra, including in situ ones, were collected on Bruker Invenio s. Each sample was mixed with KBr and examined in the wavenumber range of 4000-400 cm^{-1}. Raman spectra were collected on LabRAM HR Evolution (HORIBA, France), with a 532-nm laser, corrected using Si single crystal. A scanning electron microscope (SU8020, Hitachi, Japan) was used to observe the morphology of the samples. Transmission electron microscopy (TEM) images and high-resolution TEM (HR-TEM) images were recorded by JEM-2100F (JEOL, Japan) and JEM-1011 (JEOL, Japan). Thermogravimetric (TG) analysis was carried on TGA 4000 (PerkinElmer, United States of America), from room temperature to 600 °C at a rate of 5 °C/min. Derivative thermogravimetry (DTG) curve was drawn by differentiate the TG curve.

Synchrotron radiation[1] (SR)-based SAXS/XRD/XAFS combined technique[2] developed in the beamline 1W2B of Beijing synchrotron radiation facility (BSRF) was used to in-situ monitor the chemical reaction process. The storage ring is usually run at 2.5 GeV with an electron-beam current of about 250 mA. The X-ray photon flux is about 1.0×10^{12} photons/s at Cu K-edge (8979 eV) with an X-ray spot size of about 0.8 (H) × 0.5 (V) mm^2 at sample position. Si(111) monochromator with energy resolution (ΔE/E) of about 2×10^{-4} is equipped in the beamline 1W2B, which has an energy range of 5 ~ 18 keV.

In situ FTIR was carried out with customized single-cell-type accessary (fig. S26) on Bruker Invenio s. Attenuate total reflectance (ATR) mode with 10-time reflection to enhance signal was adopted with germanium single crystal. All the potentials from -0.1 to -1.1 V measured were not compensated by the iR compensation module.

In-situ Raman measurements were carried out using a Horiba LabRAM HR Evolution Raman microscope in a modified flow cell (purchased from Gaossunion Technology Co., Ltd.). A 785-nm laser was used and signals were recorded using a 10 s integration and by averaging 5 scans. All the potentials measured were not compensated by the iR compensation module.

Electrochemical measurements

CHI-660e electrochemical workstation was used to perform electrochemical experiments. In this work, the potentials measured by the reference electrode (RE, Ag/AgCl for in situ FTIR, Raman, XAS measurements and Hg/HgO for other electrochemical related measurement) were converted to the RHE scale based on the formula:

$$E(RHE) = E(RE) + \Delta E + 0.0592 \times pH,$$

where ΔE is 0.197 V for Ag/AgCl or 0.098 V for Hg/HgO.

CO_2ER product analysis

The products from CO_2ER were analyzed by gas chromatography (GC) and ^{1}H NMR analysis over a certain electric amount of 100 C at various potentials. Gaseous products were collected from the flow gas every 10 min, and 2 mL of the collected gas was analyzed by GC (HP 4890D) equipped with FID and TCD detectors and Argon (99.999%) as the carrier gas. The quantitative analysis was conducted based on the calibration curves of a series of standard samples at 1.013 bar and 300 K. 100 μl liquid product collected from the mixture of catholyte and anolyte was analyzed by ^{1}H NMR on Bruker AVANCE AV III 400 in 400 μl D_2O with dimethyl sulfoxide (DMSO) as internal standard.

FE of products was calculated as follows:

$$FE = (amount\ of\ M \times n \times F/C) \times 100\%$$

where M is the corresponding products, n is the number of moles of electrons participating in Faraday reaction (12 for ethanol and ethylene, 2 for CO and H_2 and 8 for methane), F is Faraday's constant (96485 C mol^{-1}), and C is the amount of charge passing through the working electrode.

Computational methods

Charge distribution calculation of SDS anion and hydroxide anion was performed using Gaussian 16 package[3]. The structures were optimized at B3lyp-6-311g(d,p) level, followed by NBO analysis[4].

The non-spin polarized DFT calculations were performed with the Vienna ab initio simulation package (VASP) program[5]. The projector augmented wave method and generalized gradient approximation of Perdew, Burke, and Ernzerh of (GGA-PBE)[6] were applied to describe the exchange-correlation functionals.

To explain the stability of SDS on Cu, auxiliary Na atoms were introduced since its electronegativity is lower than Cu and electron will migrate from Na to Cu causing an electron-rich (cathodic) environment.

The computational hydrogen electrode (CHE) approach[7] was adopted for thermodynamic analysis of the reaction pathway. In the CHE model based on the standard hydrogen electrode (SHE) reference potential, the standard chemical potential (μ^0) for a single proton-coupled electron-transfer process is defined as half of the chemical potential of a single hydrogen molecule:

$$\mu^0(H^+) + \mu^0(e^-) = 0.5\,\mu^0(H_2)$$

Gibbs free energies (G) of all reaction intermediates at zero potential are defined as:

$$G = E_{DFT} + \Delta ZPE - TS$$

where E_{DFT} is the calculated energy, ΔZPE is the correction of zero-point energy (ZPE), and $-TS$ is the entropy correction[8].*CO and unabsorbed CO, *CO+*CO, *CHCHO, *CCO, *HCCOH, *HCCOH, *HCCHOH, *CH_2CHOH, *CH_2CH_2OH, *CCH, *CCH_2, *$CHCH_2$ pathways were evaluated with adsorption energies on Cu(111), and propyl sulfonate modified Cu(111) (Cu@PS) (Figures 4a and 4b, Table S1), whereas $CH_3CH_2OH + H_2O$ is set as final state. Taking reaction energy of *HCCOH as instance, the result = G(*HCCOH) + G(H_2O) + 2*G(H_2), since after 4 proton-coupled electron-transfer process *HCCOH will turn into CH_3CH_2OH, while H_2O and H_2 are used for mass balance . A vacuum space of 14 Å was retained to avoid interactions between periodic atoms along the z-direction. The slab models were fully relaxed to reach a convergence criterion of 10^{-5} eV in total energy and 0.01 eV/Å in residual forces. The cutoff energy was set to 400 eV. A 2 × 2 × 1 Monkhorst-Pack k-point mesh was adopted for all calculations. The pre- and post-processing data were produced by VASPKIT [9].

Charge density difference was calculated by formula:

$$\Delta\rho = \rho_{AB} - \rho_A - \rho_B$$

where AB equals to Cu(111)@PS, A equals to PS, B equals to Cu(111).

Results and Discussion

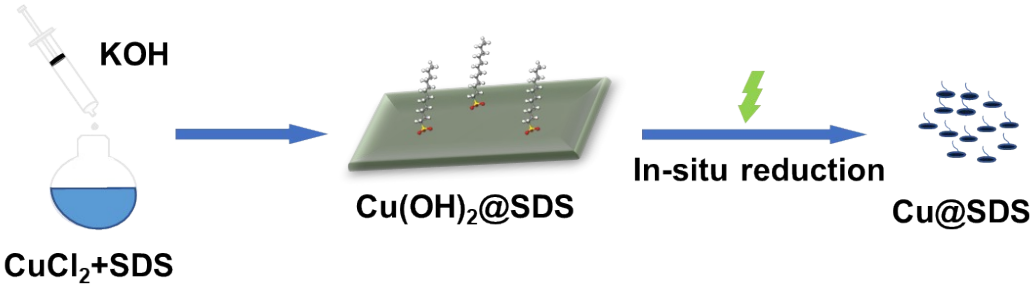

Figure S1. Illustration of Cu@SDS preparation.

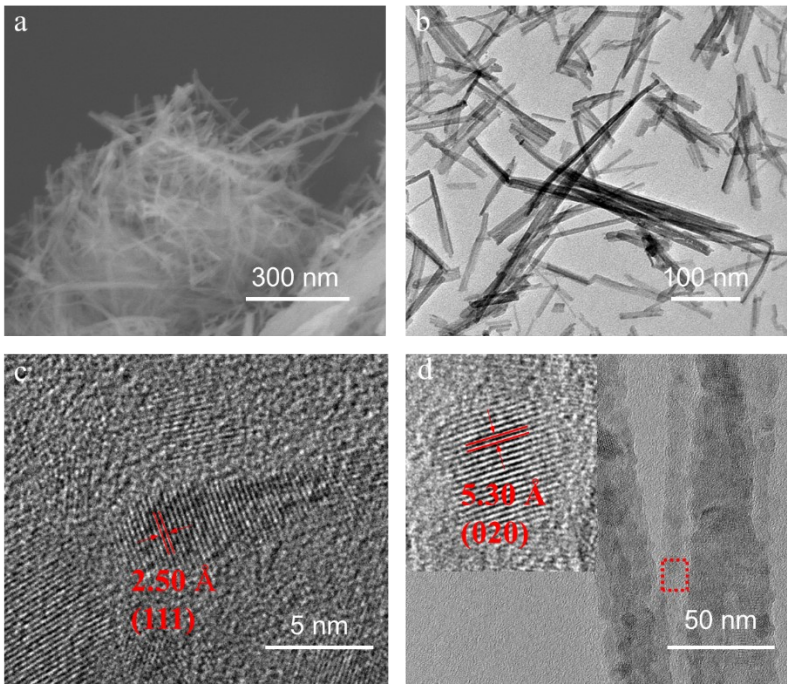

Figure S2. (a) SEM image, (b) TEM image and (c, d) HR-TEM images of $Cu(OH)_2$@SDS.

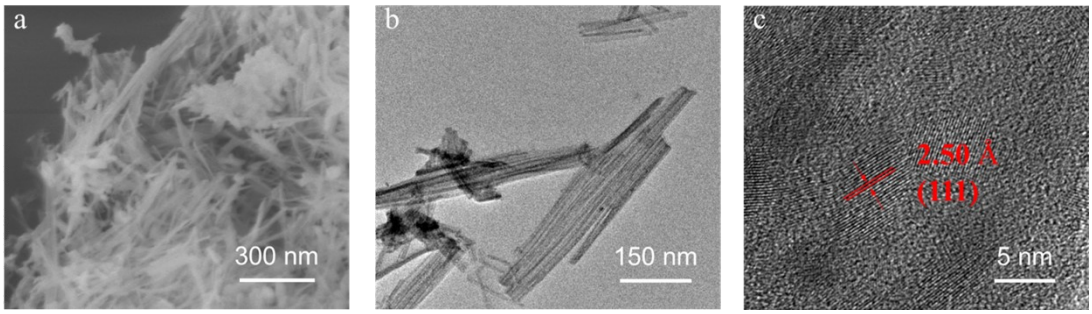

Figure S3. (a) SEM image, (b) TEM image and (c) HR-TEM image of $Cu(OH)_2$.

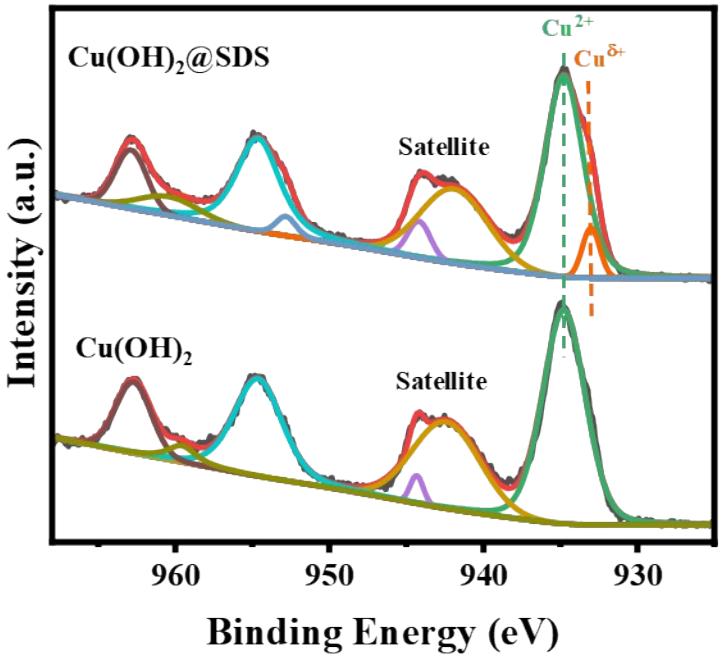

Figure S4. Cu 2p X-ray photoelectron spectroscopy (XPS) of $Cu(OH)_2$@SDS and $Cu(OH)_2$. $Cu(OH)_2$ exhibits a single peak at 934.7 eV in the Cu 2p XPS spectrum, corresponding to Cu^{2+}.[10] In comparison, an additional peak appears at 933.0 eV for $Cu(OH)_2$@SDS, indicating the presence of $Cu^{\delta+}$. Thus, we deduce that DS anion replaces the superficial OH^- in $Cu(OH)_2$, and a larger ion radius causes hindrance for interaction between OH^- and Cu^{2+}, resulting in a lower oxidation state of copper.

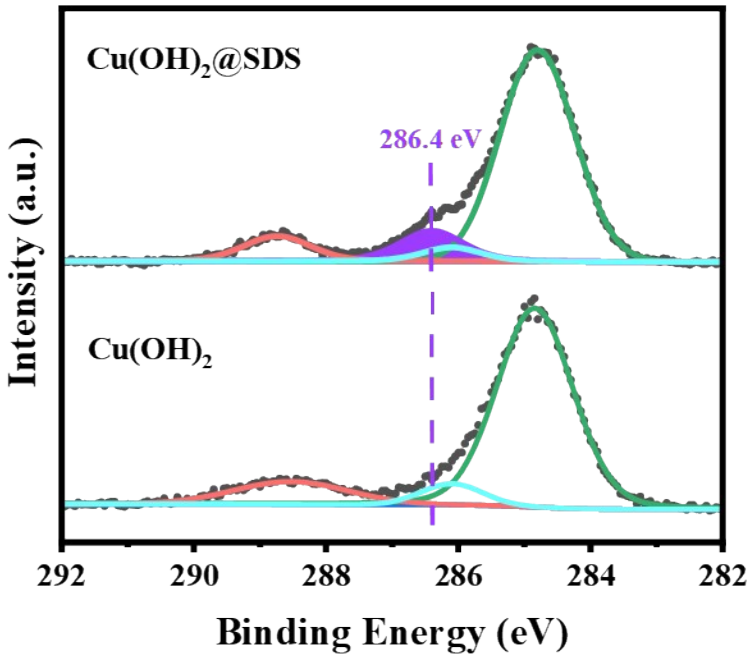

Figure S5. C 1s XPS of $Cu(OH)_2$@SDS and $Cu(OH)_2$. An additional peak appears at 256.4 eV, which could be assigned to carbon in SDS alkyl group, indicating the existance of SDS on the surface of $Cu(OH)_2$@SDS.

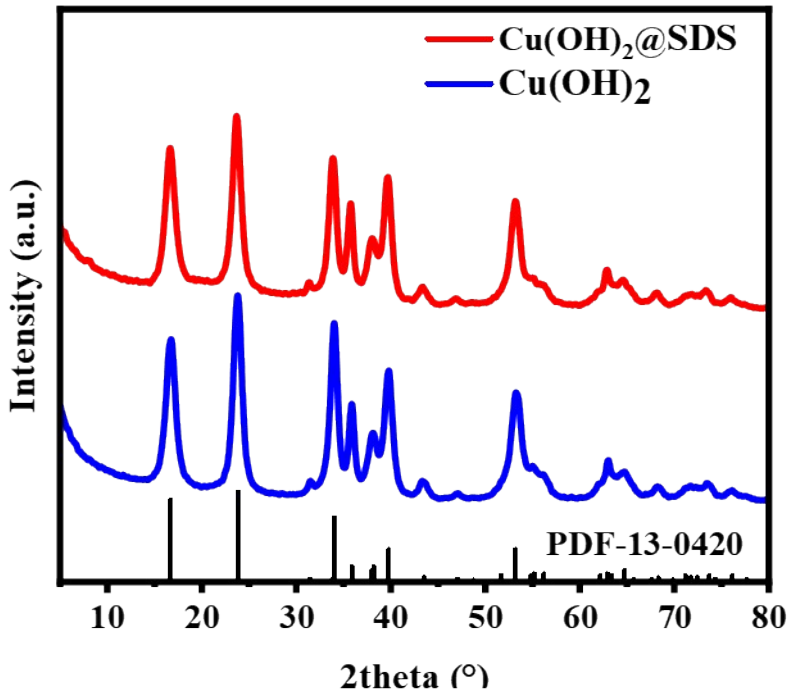

Figure S6. XRD patterns of $Cu(OH)_2$@SDS and $Cu(OH)_2$. Clearly, these two samples display similar XRD patterns, suggesting SDS does not modify the crystalline structure of $Cu(OH)_2$ in $Cu(OH)_2$@SDS.

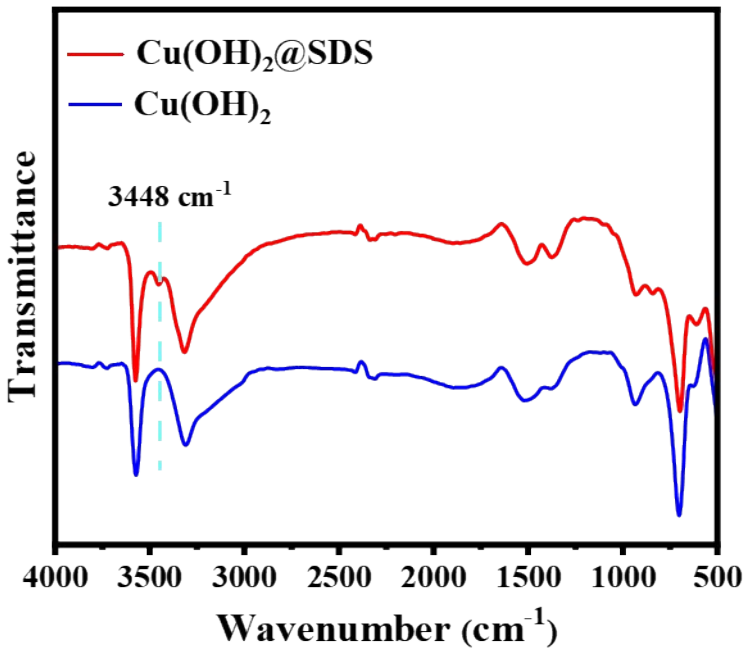

Figure S7. FTIR spectra of $Cu(OH)_2$@SDS and $Cu(OH)_2$. A peak appears at 3448 cm^{-1} in the FTIR spectrum of $Cu(OH)_2$@SDS, while it does not appear in that of $Cu(OH)_2$[11]. This band may be ascribed to the stretching vibration of O-H of $Cu(OH)_2$ complexed with SDS, providing the evidence for the presence of SDS in the $Cu(OH)_2$@SDS catalyst. The absence of signals assigning to CH_2 may be ascribed to the trace amount of SDS.

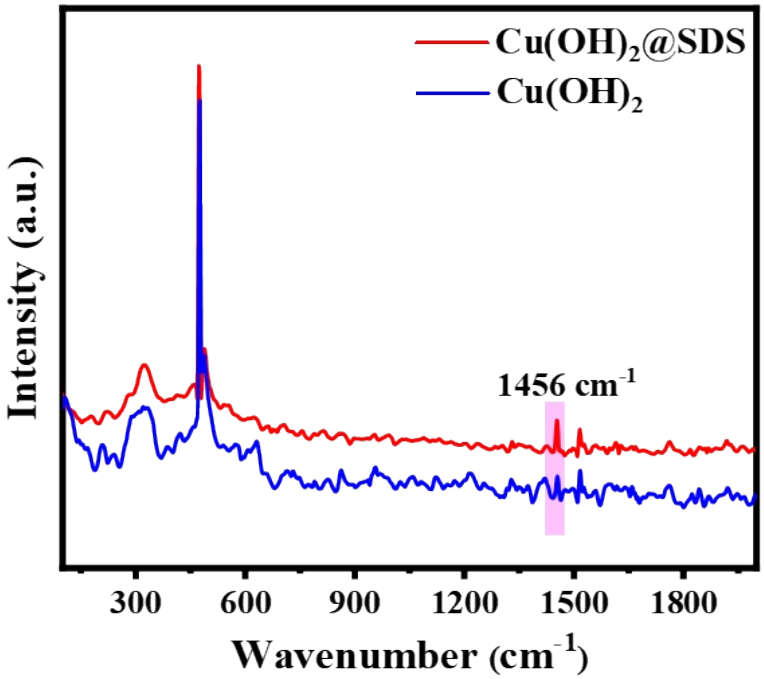

Figure S8. Raman spectra of $Cu(OH)_2$@SDS and $Cu(OH)_2$. Characteristic stretching vibrations associated with the alkyl chain like -CH_2- or -CH_3 are observed at 1456 cm^{-1} in the Raman spectra, distinct from the characteristic peak at 488 cm^{-1} observed for $Cu(OH)_2$[12].

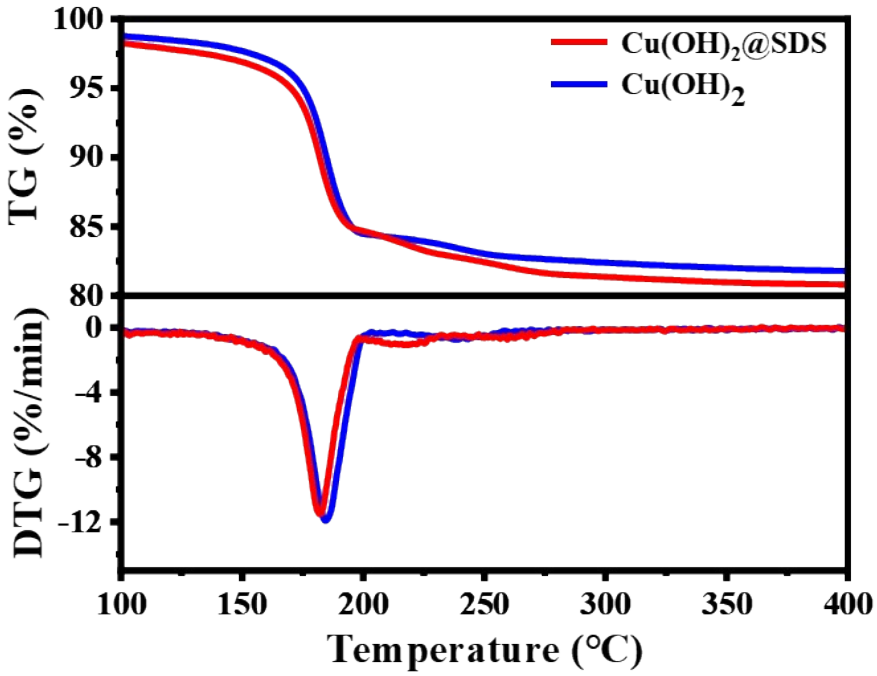

Figure S9. TG and DTG curves of $Cu(OH)_2$@SDS and $Cu(OH)_2$. It is demonstrated that the SDS content in the $Cu(OH)_2$@SDS sample was about 0.5 wt%.

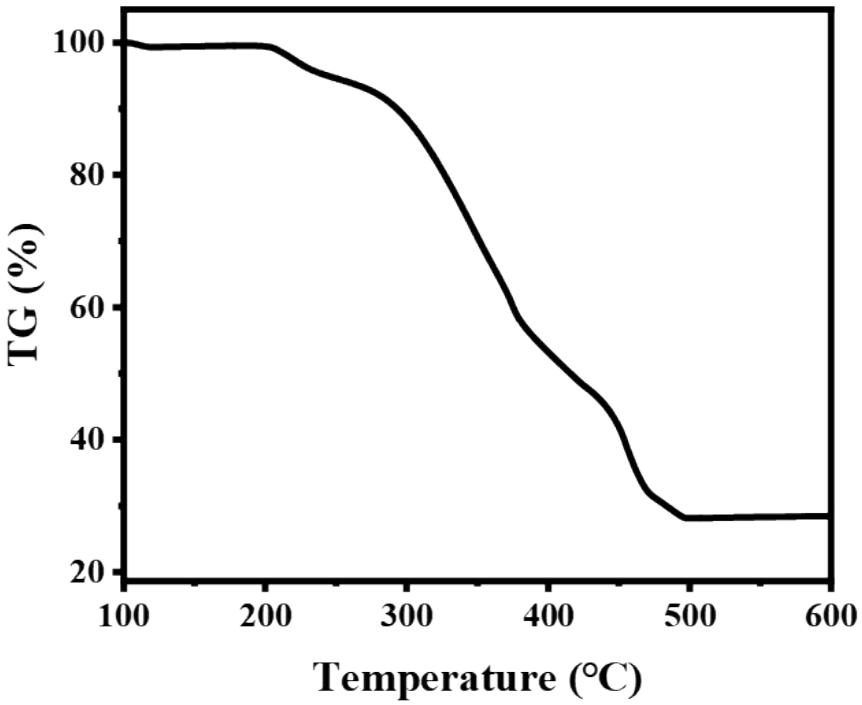

Figure S10. TG analysis curve of SDS.

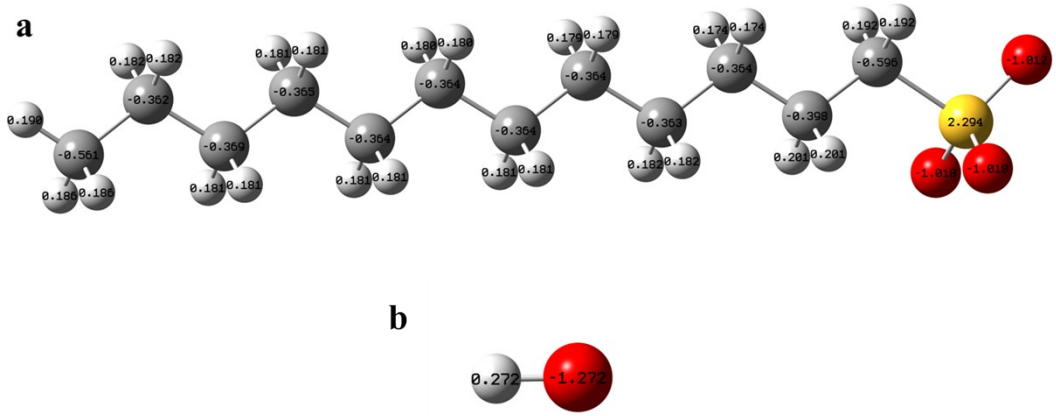

Figure S11. Charge distribution of (a) DS^- and (b) OH^-. The average charge on O in DS^- is -1.016 e, while in OH^- it is -1.272 e. A larger ion radius causes hindrance for interaction between OH^- and Cu^{2+}, resulting in a lower oxidation state of copper (Figure S3).

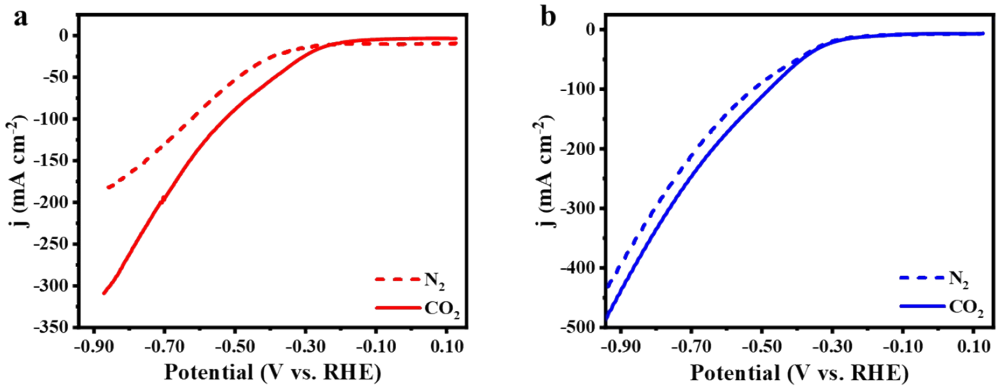

Figure S12. LSV comparison of Cu@SDS (a) and OHDCu (b) under N_2 or CO_2.

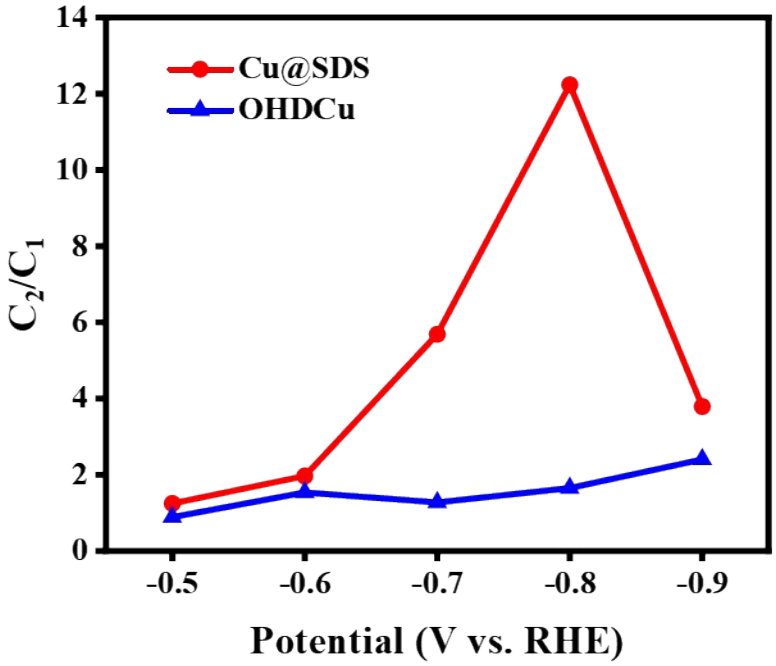

Figure S13. The ratios of C_2/C_1 over Cu@SDS and OHDCu at different potentials.

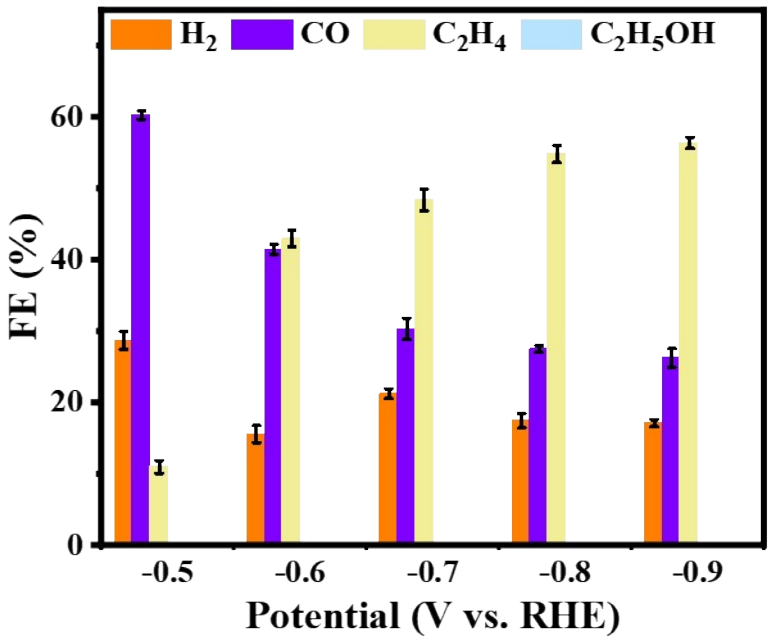

Figure S14. FEs of the products from CO_2ER over mechanically mixed SDS and $Cu(OH)_2$ at different potentials.

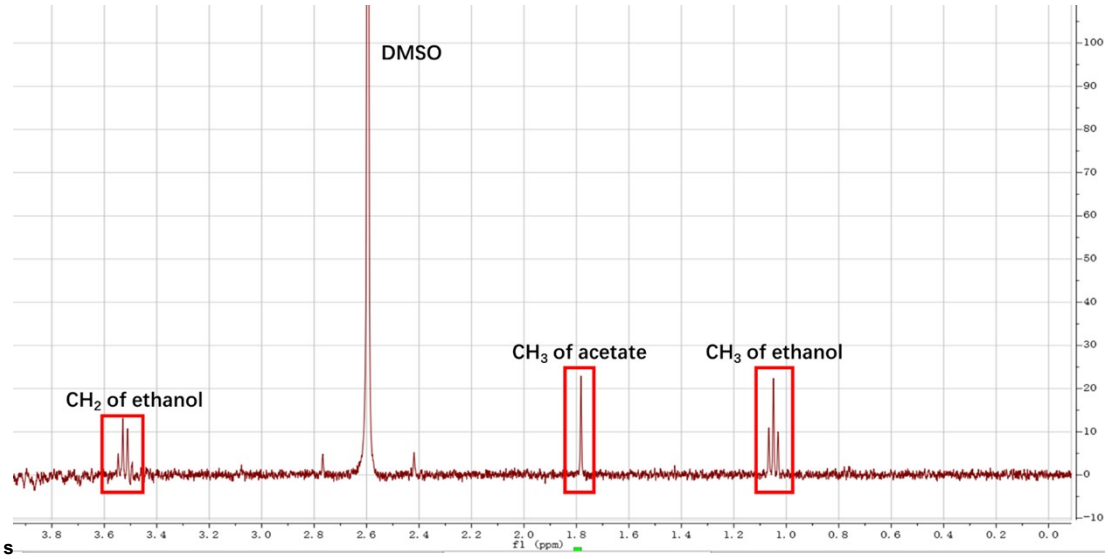

Figure S15. ^{1}H NMR spectrum of liquid products of CO_2ER over Cu@SDS at 100 mA cm^{-2} for 3 h. Acetate was generated from the oxidation of ethanol that diffused from catholyte to anolyte, which was included in FEs calculation of ethanol.

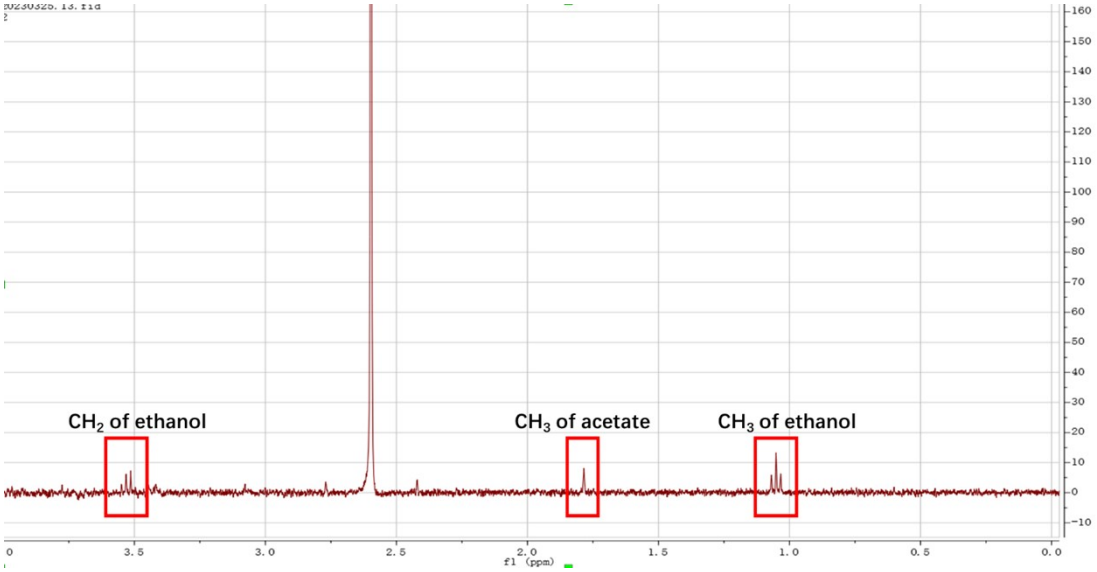

Figure S16. ^{1}H NMR spectrum of the anolyte with addition of ethanol into catholyte only, applying current density at 100 mA cm^{-2} for 3 h. The presence of peak assigned to acetate in ^{1}H NMR spectrum indicates that ethanol can diffuse from catholyte to anolyte and be oxidized to acetate.

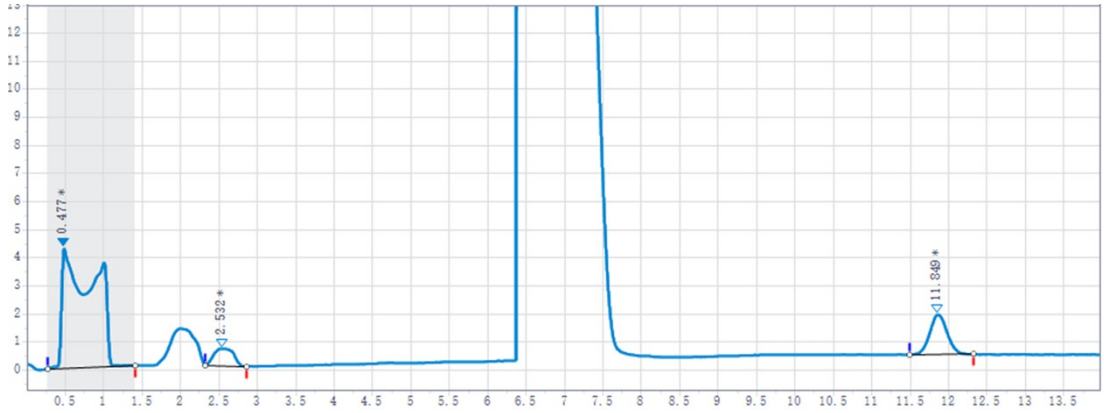

Figure S17. GC spectrum of the gas phase of CO_2ER over Cu@SDS at applied potential of -0.8 V. Peaks from the left to the right are assigning to H_2, air, CO, CO_2 and ethylene.

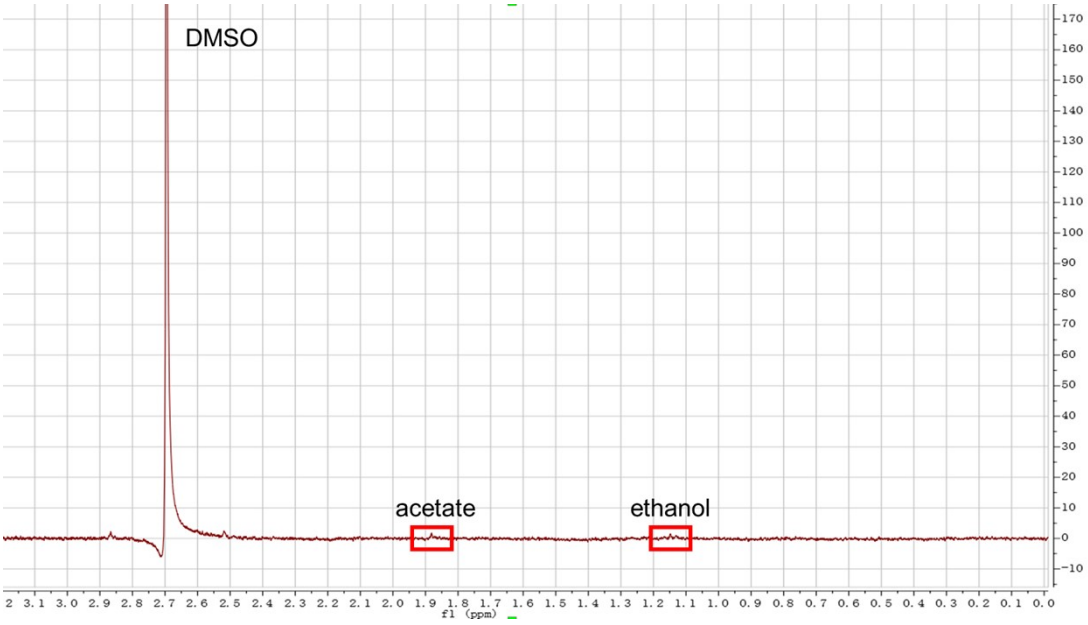

Figure S18. ^{1}H NMR spectrum of liquid products of CO_2ER over Cu@SOS at -0.8 V. Trace amounts of ethanol and acetate were detected.

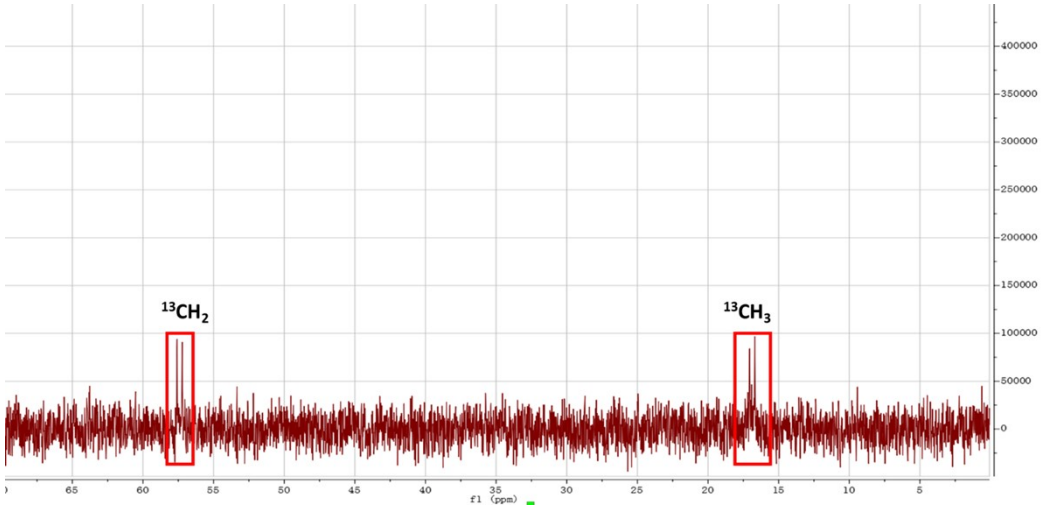

Figure S19. ^{13}C NMR spectrum of liquid products with $^{13}CO_2$ as feedstock over Cu@SDS at -0.8 V.

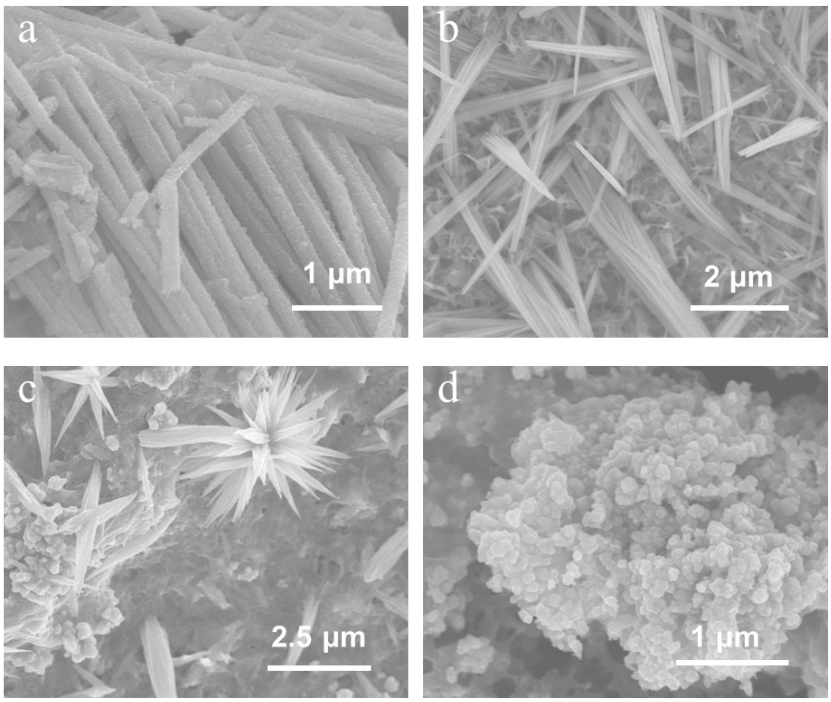

Figure S20. SEM images of the catalysts evolved from $Cu(OH)_2$@SDS to Cu@SDS via electroreduction for desired time at -0.7 V. (a) fresh $Cu(OH)_2$@SDS, (b) electroreduction for 10 s, (c) electroreduction for 20 s, (d) electroreduction for 30 s. From these SEM images, it is clearly that the nanorod-like morphology of $Cu(OH)_2$@SDS gradually transformed into stacked irregular nanoparticles.

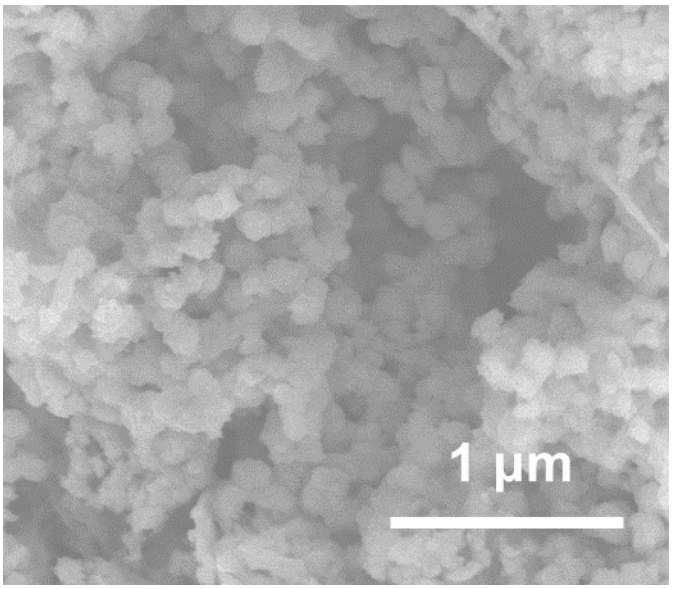

Figure S21. SEM image of OHDCu.

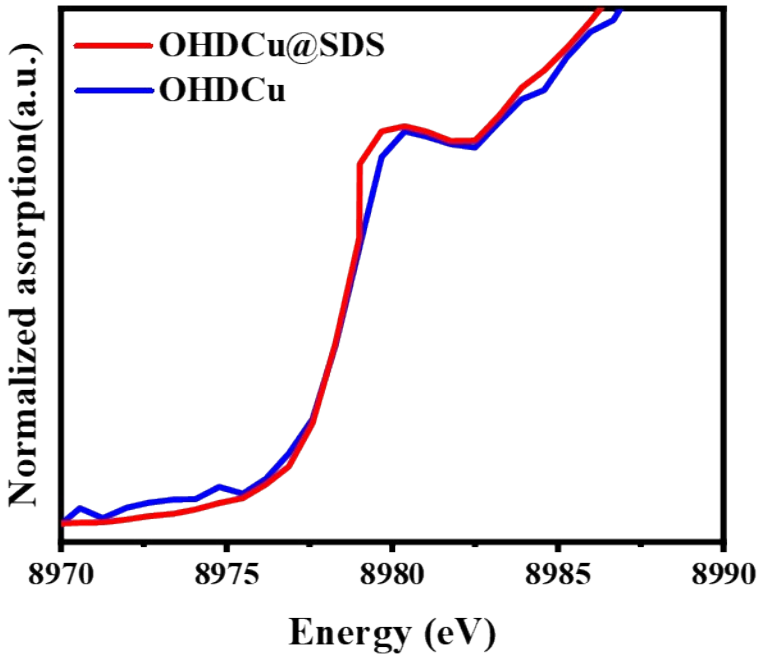

Figure S22. XANES of Cu@SDS and OHDCu applied in CO_2ER at -0.9 V.

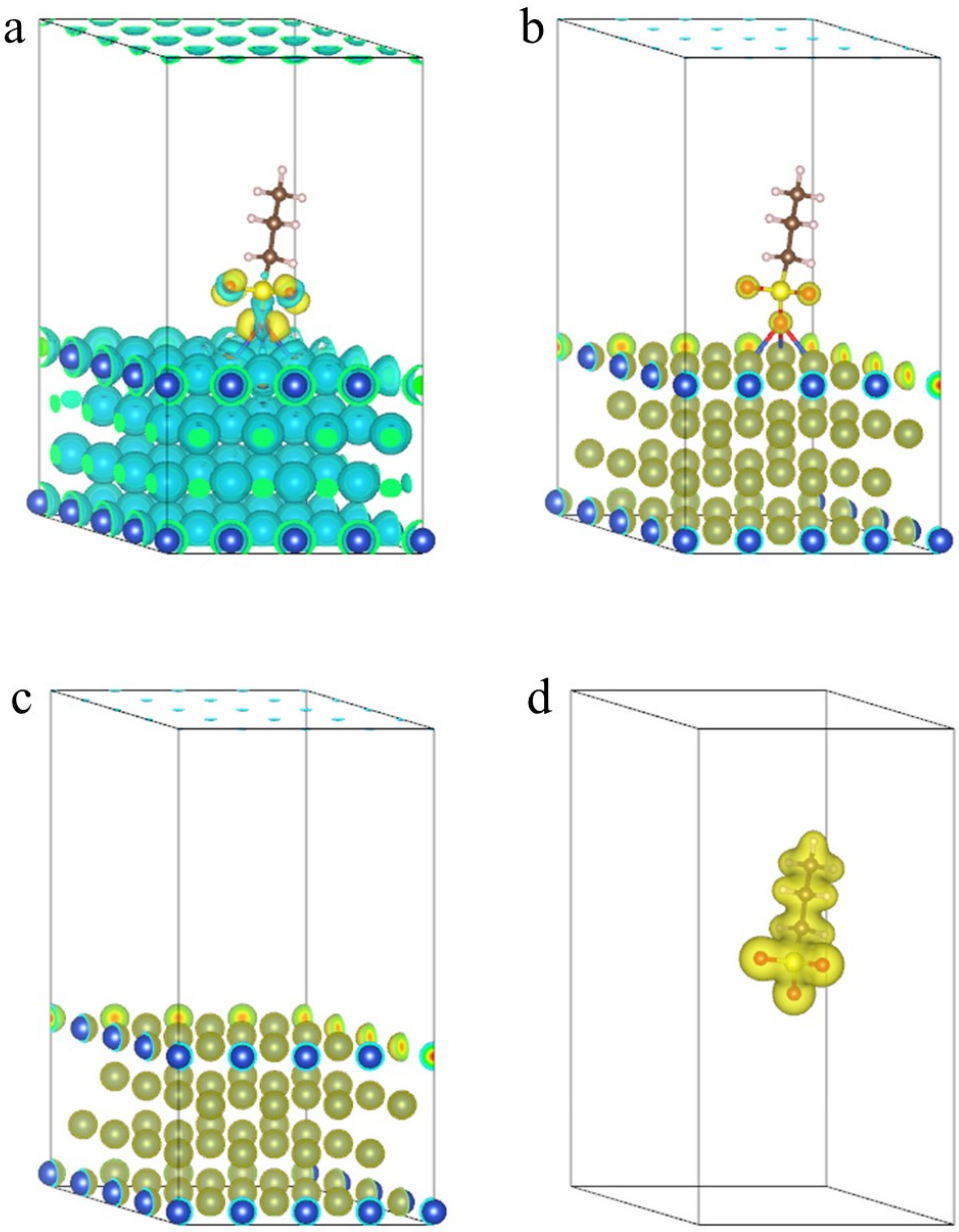

Figure S23. Difference charge density analysis given in isosurface graph. (a) Cu(111)@PS from Cu(111) and PS. (b) Charge distribution of Cu(111)@PS, (c) Cu(111) and (d) PS. The yellow and cyan isosurfaces show the charge gained and lost regions, respectively, corresponding to positive and negative values in the curve charts. Blue, red, brown, yellow and grey spheres represent Cu, O, C, S and H atoms, respectively.

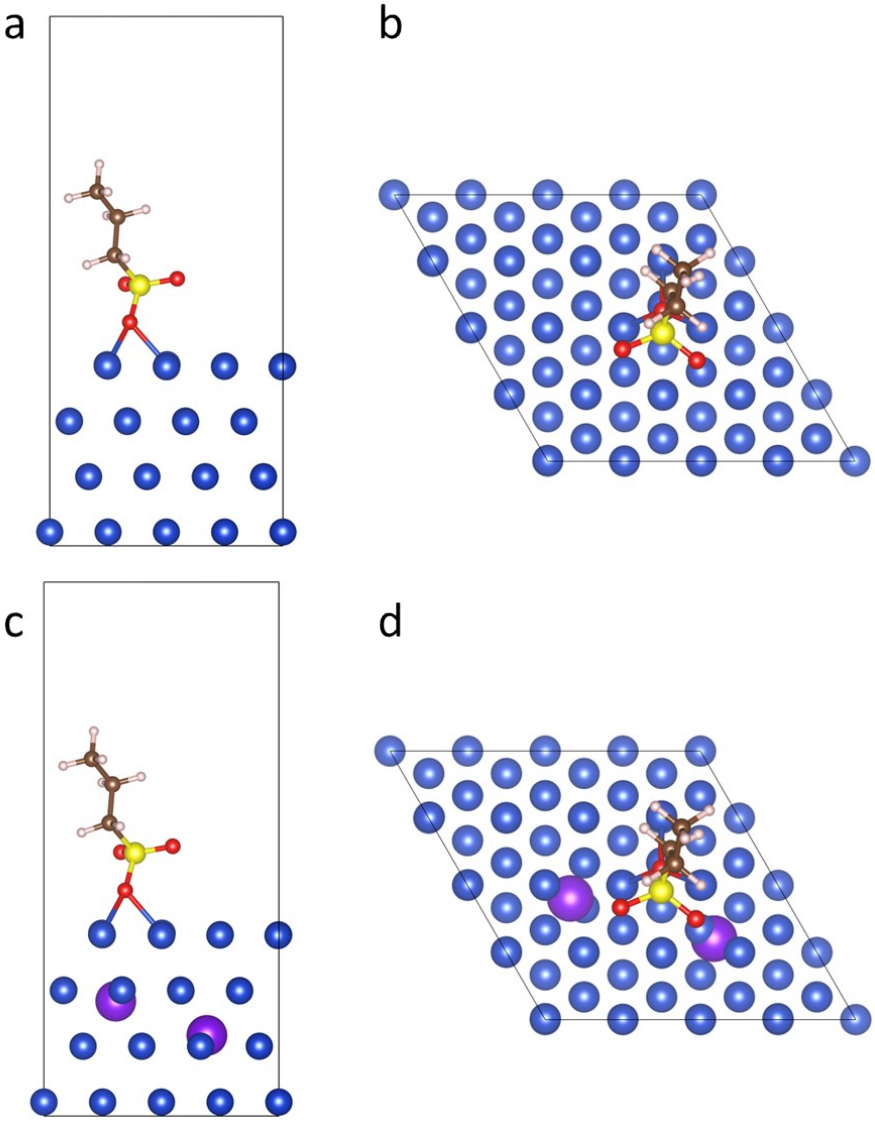

Figure S24. Structure of Cu(111)@PS before (a from ***b*** direction and b from ***c*** direction) and after (c from ***b*** direction and d from ***c*** direction) anchoring 2 Na atoms into Cu structure. Bond length of Cu-O coordinate between direct absorbed O from SDS and nearest three Cu atoms are 2.12372, 2.38248 and 2.14925 Å (average 2.22 Å) respectively, while the lengths before Na introduced are 2.14760, 2.13373 and 2.36010 Å (average 2.21 Å). Blue, red, brown, yellow, purple and grey spheres represent Cu, O, C, S, Na and H atoms, respectively.

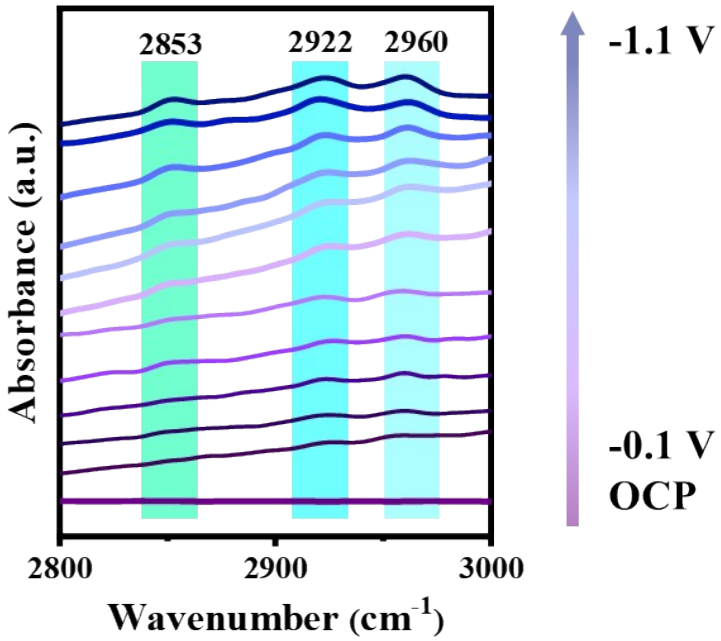

Figure S25. In situ FTIR spectra from 2800 cm^{-1} to 3000 cm^{-1} applying Cu@SDS as catalyst with potential applied from OCP, -0.1 V to -1.1 V.

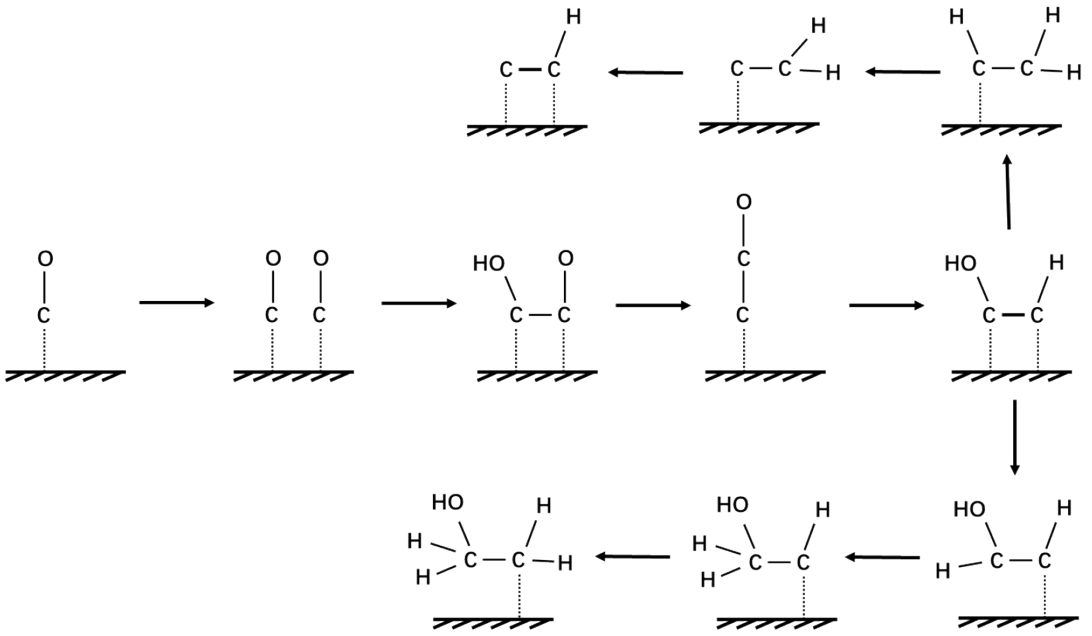

Figure S26. Circumstantial catalytic route towards ethanol (lower) or ethylene (upper) generation on Cu@SDS or OHDCu.

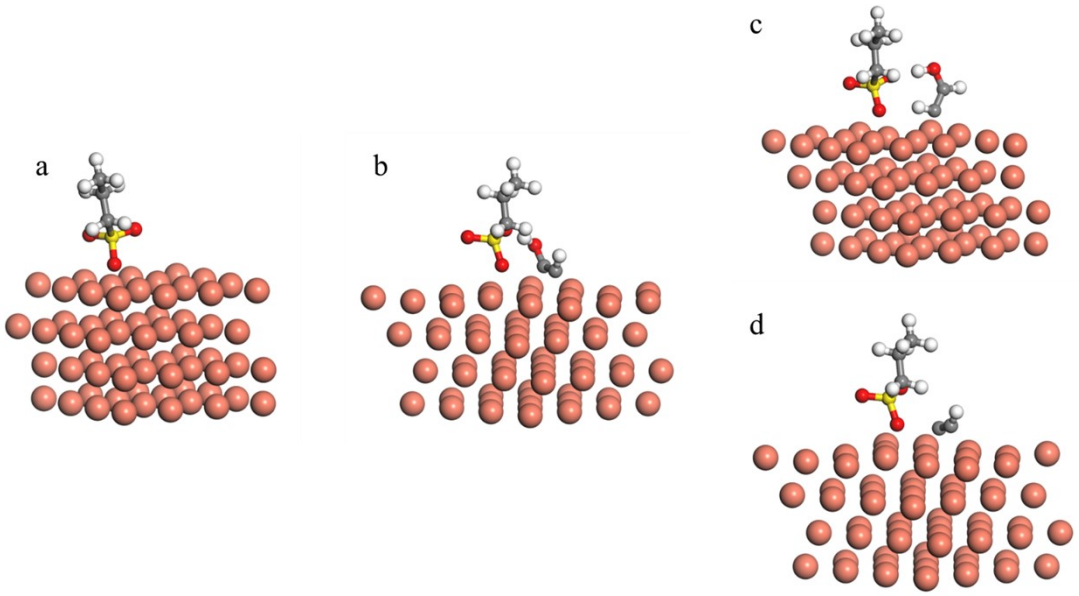

Figure S27. Full version of reaction paths on Cu(111)@PS. (a) Cu(111)@PS, (b) Cu(111)@PS*HCCOH, (c) Cu(111)@PS*HCCHOH and (d) Cu(111)@PS*CCH. Orange, red, brown, yellow and grey spheres represent Cu, O, C, S and H atoms, respectively.

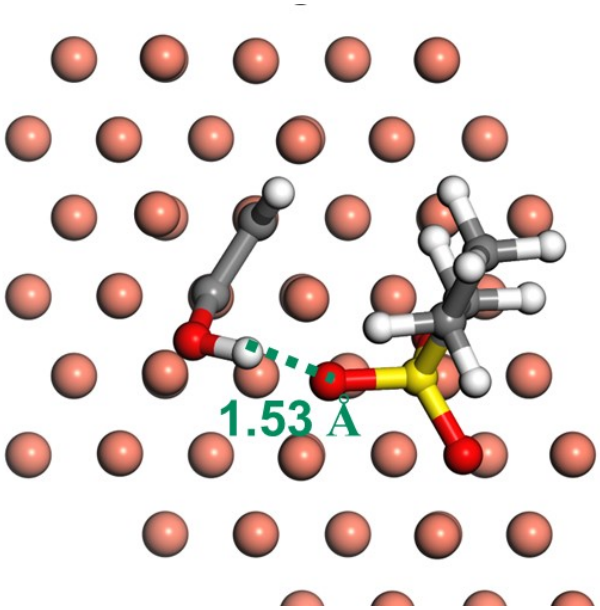

Figure S28. Distance between H in *HCOOH and O from SDS.

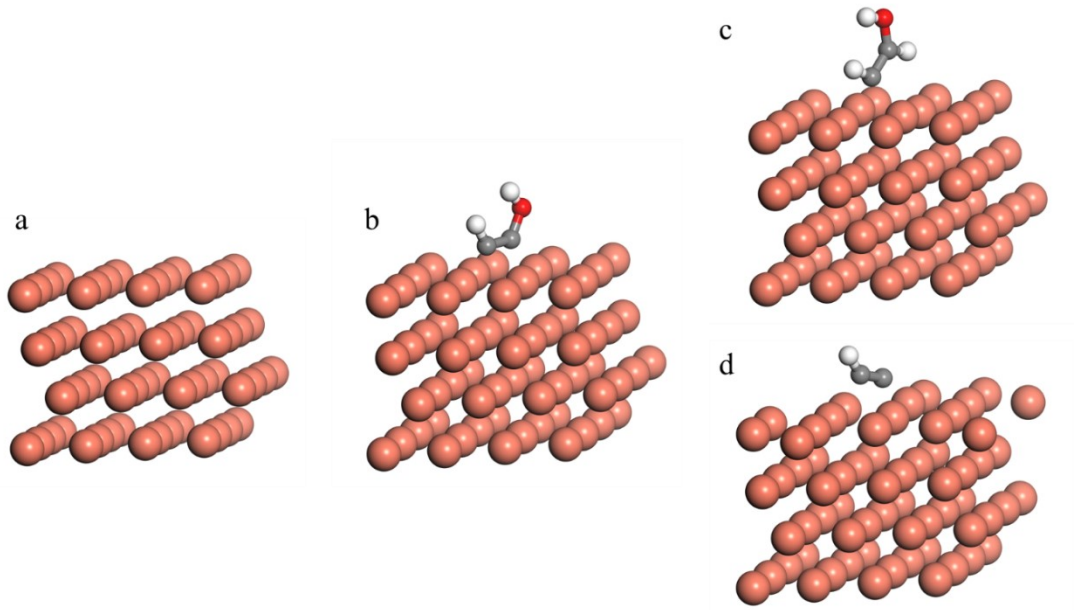

Figure S29. Full version of reaction paths on Cu(111). (a) Cu(111), (b) Cu(111)*HCCOH, (c) Cu(111)*HCCHOH and (d) Cu(111)*CCH. Orange, red, brown, yellow and grey spheres represent Cu, O, C, S and H atoms, respectively.

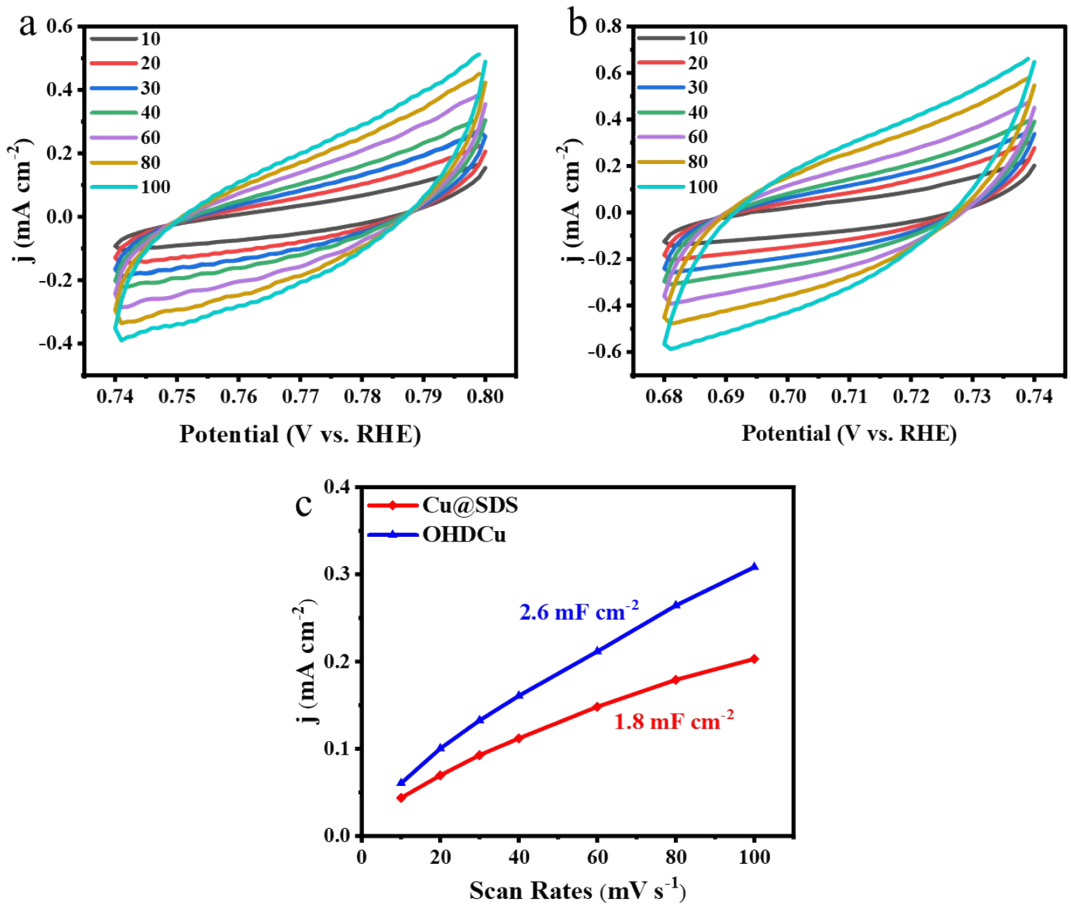

Figure S30. Cyclic voltammograms of Cu@SDS (a) and OHDCu (b). A higher open circuit potential is observed, which also gives evidence that Cu@SDS possess a higher Cu chemical state. (c) Calculated C_{dl} according to (a, b). The ECSA of the working electrode was calculated according to the following formula:

$$ECSA = R_f \times S$$

where S is the actual surface area of the working electrode, and R_f is the roughness factor of the working electrode. S is equal to the geometric area of the working electrode (in this work, S=1 cm^2), and R_f can be calculated by the relation $R_f = C_{dl}/a$. C_{dl} was first determined because ECSA is proportional to the C_{dl} value. The capacitive currents associated with double-layer charging associated with the scan rate of CV were measured in the range from 0.68 to 0.74 V for OHDCu and 0.74 to 0.80 for Cu@SDS under the same conditions. The scan rates were set at 10, 20, 30, 40, 60, 80 and 100 mV s^{-1}. Cdl was estimated by plotting the relationship of Δj (j_a-j_c) at 0.61 V or 0.77 V with the scan rates, where j_a and j_c are the anode and cathode current densities, respectively. We used a pure copper sheet with a roughness factor of 1 (C_{Cu} = 29 μF) to normalize the ECSA of all samples. ECSA of Cu@SDS and OHDCu was determined to be 62 and 89 cm^2, respectively. This figure explains the reason why the current density is lower applying Cu@SDS as catalyst than OHDCu.

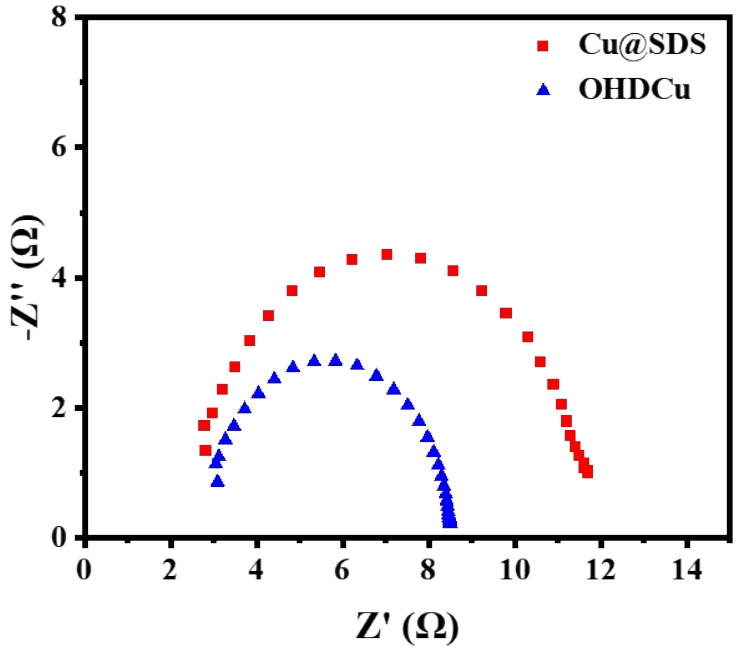

Figure S31. The EIS data of Cu@SDS and OHDCu. EIS was performed at open circuit potential (OCP) with a frequency range of 10-10^5 Hz and an amplitude of 5 mV.

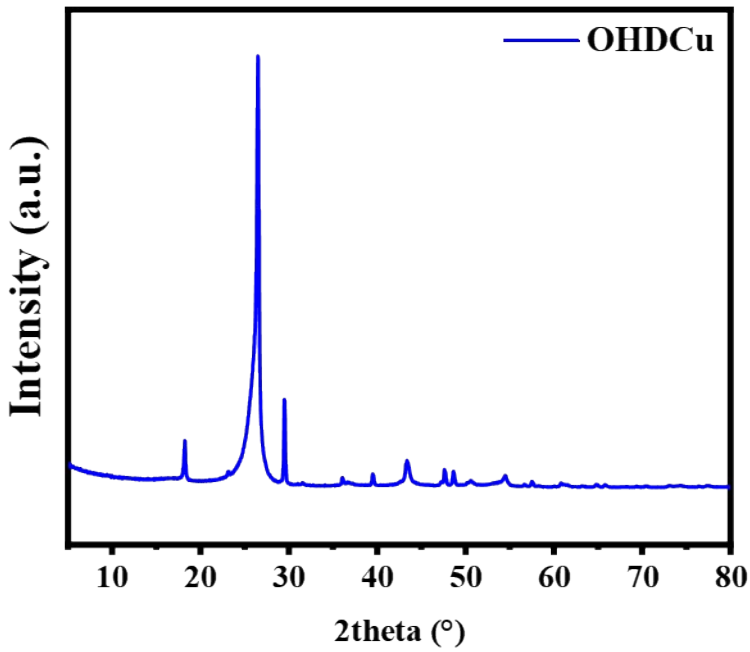

Figure S32. XRD pattern of OHDCu on Nafion-contained carbon paper.

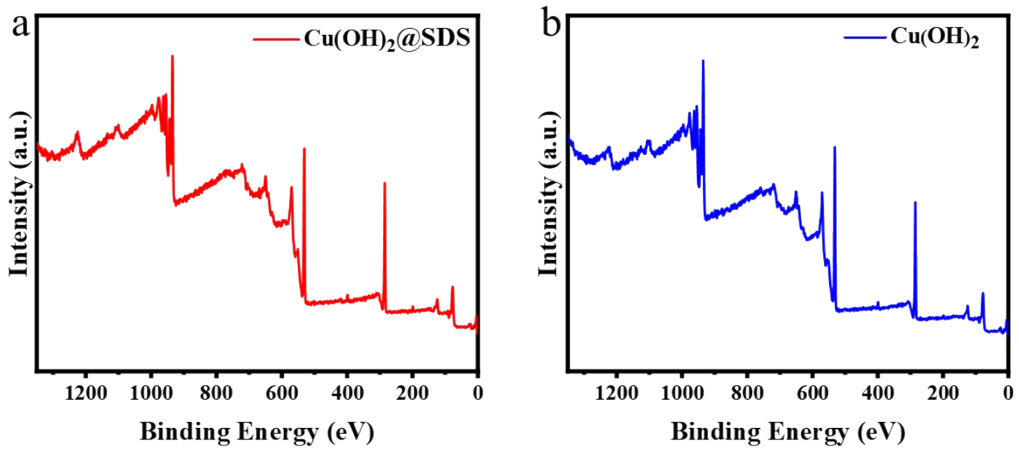

Figure S33. XPS survey of $Cu(OH)_2$@SDS (a) and $Cu(OH)_2$ (b).

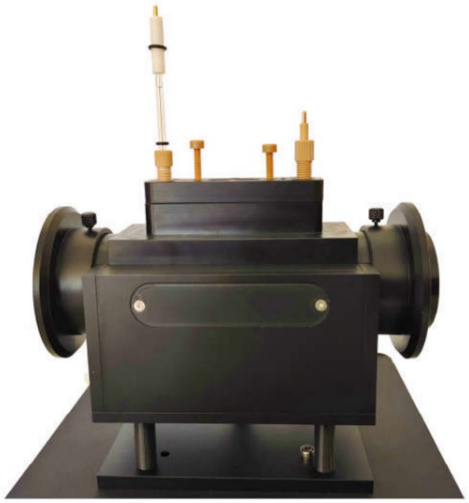

Figure S34. Picture of customized in situ FTIR accessary of ATR mode.

Table S1. Calculated energies of slabs and with adsorbed species[a].

Entry	Slab	*CO	*CO*CO	*COCOH	*CCO	*CHCOH
Cu(111)	-224.15	-281.79	-281.89	-280.86	-282.24	-281.89
Cu(111)@PS	-301.57	-356.43	-359.48	-335.63	-358.84	-359.56
Entry	*CCH	*CCH_2	*$CHCH_2$	*ethylene	ethylene molecule	ethanol molecule
Cu(111)	-285.56	-282.44	-282.76	-283.32	-30.72	-44.91
Cu(111)@PS	-362.81	-360.36	-360.30	-360.74		
Entry	*CHCHOH	*CH_2CHOH	*CH_2CH_2OH	ethanol	H_2O molecule	H_2 molecule
Cu(111)	-285.01	-282.54	-282.39	-283.29	-14.23	-6.80
Cu(111)@PS	-363.49	-360.61	-360.02	-360.71		

[a] Unit of energies is eV.

Reference

1. Wu, Z.; Sheng, W.; Liu, Y., Synchrotron Radiation and Its Applications in Inorganic Materials. *Journal of Inorganic Materials* **2021,** *36* (9).
2. Wu, Z.; Liu, Y.; Xing, X.; Yao, L.; Chen, Z.; Mo, G.; Zheng, L.; Cai, Q.; Wang, H.; Zhong, J.; Lai, Y.; Qian, L., A novel SAXS/XRD/XAFS combined technique for in-situ time-resolved simultaneous measurements. *Nano Research* **2022,** *16* (1), 1123-1131.
3. Frisch, M. J.; Trucks, G. W.; Schlegel, H. B.; Scuseria, G. E.; Robb, M. A.; Cheeseman, J. R.; Scalmani, G.; Barone, V.; Petersson, G. A.; Nakatsuji, H.; Li, X.; Caricato, M.; Marenich, A. V.; Bloino, J.; Janesko, B. G.; Gomperts, R.; Mennucci, B.; Hratchian, H. P.; Ortiz, J. V.; Izmaylov, A. F.; Sonnenberg, J. L.; Williams; Ding, F.; Lipparini, F.; Egidi, F.; Goings, J.; Peng, B.; Petrone, A.; Henderson, T.; Ranasinghe, D.; Zakrzewski, V. G.; Gao, J.; Rega, N.; Zheng, G.; Liang, W.; Hada, M.; Ehara, M.; Toyota, K.; Fukuda, R.; Hasegawa, J.; Ishida, M.; Nakajima, T.; Honda, Y.; Kitao, O.; Nakai, H.; Vreven, T.; Throssell, K.; Montgomery Jr., J. A.; Peralta, J. E.; Ogliaro, F.; Bearpark, M. J.; Heyd, J. J.; Brothers, E. N.; Kudin, K. N.; Staroverov, V. N.; Keith, T. A.; Kobayashi, R.; Normand, J.; Raghavachari, K.; Rendell, A. P.; Burant, J. C.; Iyengar, S. S.; Tomasi, J.; Cossi, M.; Millam, J. M.; Klene, M.; Adamo, C.; Cammi, R.; Ochterski, J. W.; Martin, R. L.; Morokuma, K.; Farkas, O.; Foresman, J. B.; Fox, D. J. *Gaussian 16 Rev. C.01*, Wallingford, CT, 2016.
4. Glendening, E. D.; Landis, C. R.; Weinhold, F., Natural bond orbital methods. *WIREs Computational Molecular Science* **2011,** *2* (1), 1-42.
5. Hafner, J., Ab-initio simulations of materials using VASP: Density-functional theory and beyond. *J. Comput. Chem.* **2008,** *29* (13), 2044-78.
6. Perdew, J. P.; Burke, K.; Ernzerhof, M., Generalized Gradient Approximation Made Simple [Phys. Rev. Lett. 77, 3865 (1996)]. *Phys. Rev. Lett.* **1997,** *78* (7), 1396-1396.
7. Nørskov, J. K.; Rossmeisl, J.; Logadottir, A.; Lindqvist, L.; Kitchin, J. R.; Bligaard, T.; Jónsson, H., Origin of the Overpotential for Oxygen Reduction at a Fuel-Cell Cathode. *The Journal of Physical Chemistry B* **2004,** *108* (46), 17886-17892.
8. Pilati, T.; Forni, A., SYMMOL: a program to find the maximum symmetry group in an atom cluster, given a prefixed tolerance. *J. Appl. Crystallogr.* **1998,** *31* (3), 503-504.
9. Wang, V.; Xu, N.; Liu, J.-C.; Tang, G.; Geng, W.-T., VASPKIT: A user-friendly interface facilitating high-throughput computing and analysis using VASP code. *Comput. Phys. Commun.* **2021,** *267*.
10. Deroubaix, G.; Marcus, P., X-ray photoelectron spectroscopy analysis of copper and zinc oxides and sulphides. *Surf. Interface Anal.* **1992,** *18* (1), 39-46.
11. Muratovic, S.; Martinez, V.; Karadeniz, B.; Pajic, D.; Brekalo, I.; Arhangelskis, M.; Mazaj, M.; Mali, G.; Etter, M.; Friscic, T.; Krupskaya, Y.; Kataev, V.; Zilic, D.; Uzarevic, K., Low-Dimensional Magnetism in Multivariate Copper/Zinc MOF-74 Materials Formed via Different Mechanochemical Methods. *Inorg. Chem.* **2022,** *61* (45), 18181-18192.
12. Mayer, S. T.; Muller, R. H., An In Situ Raman Spectroscopy Study of the Anodic Oxidation of Copper in Alkaline Media. *J. Electrochem. Soc.* **1992,** *139* (2), 426.